Journal of
Manufacturing and Materials Processing

MDPI

Article

Thin-Walled Part Properties in Powder Bed Fusion of Polymers—A Comparative Study on Temperature Development and Part Performance Depending on Part Thickness and Orientation

Andreas Jaksch [1,2,*], Simon Cholewa [1,2] and Dietmar Drummer [1,2]

[1] Collaborative Research Center—Additive Manufacturing (CRC 814), Friedrich-Alexander-Universität Erlangen-Nürnberg, Am Weichselgarten 10, 91058 Erlangen, Germany
[2] Institute of Polymer Technology, Friedrich-Alexander-Universität Erlangen-Nürnberg, Am Weichselgarten 10, 91058 Erlangen, Germany
* Correspondence: andreas.jaksch.de@fau.de

Abstract: To develop new areas of application for laser-based powder bed fusion of polymers (PBF-LB/P), a deeper process understanding of the resulting mechanical properties, particularly for thin-walled and complex structures, is needed. This work addresses the influence of part thickness and orientation in detail. For a general understanding, two PBF systems were used. For comparison, the normalized energy density was determined for specimens of various thicknesses and orientations. It could be seen that the normalized energy density exhibited opposing trends for the two systems for progressively thinner samples. During the process, the exposure temperature development was observed using an infrared camera for a greater understanding of the developing part properties. To further investigate the fracture behavior, an infrared camera was used during tensile testing, which revealed various patterns depending on the PBF-System used. The results showed a machine-dependent difference in the exposure temperatures and elongation at break for z-oriented parts. While the surface roughness was independent of the thickness, the density, porosity, and the mechanical properties were affected significantly by the part thickness. The parts showed a brittle breaking behavior with a crack initiation from the short side of the tensile bar. These results improved process expertise, and in particular the mechanical performance of thin-walled structures caused by temperature variations in PBF-LB/P.

Keywords: powder bed fusion; thin walled; part properties; polyamide 12; mechanical properties

Citation: Jaksch, A.; Cholewa, S.; Drummer, D. Thin-Walled Part Properties in Powder Bed Fusion of Polymers—A Comparative Study on Temperature Development and Part Performance Depending on Part Thickness and Orientation. *J. Manuf. Mater. Process.* **2023**, *7*, 96. https://doi.org/10.3390/jmmp7030096

Academic Editor: Eugene Olevsky

Received: 12 April 2023
Revised: 3 May 2023
Accepted: 9 May 2023
Published: 11 May 2023

1. Introduction

In recent years, customer demands for components have changed significantly. The industry focuses on challenges in increasing automation, networking, cloud computing, and highly dynamic manufacturing processes [1]. Additive manufacturing methods are considered key to economically reflect market dynamics and individualized components to overcome these challenges [2]. Initially, the production of plastic components using additive manufacturing was limited to prototypes and small series, but new processes, machine developments, and materials have expanded applications to series production [3].

Various manufacturing methods in polymer-based additive manufacturing have specific properties, and are suitable for different application areas [3]. In the industrial environment, Fused Deposition Modeling (FDM), Stereolithography (SLA), and Powder Bed Fusion (PBF-LB/P) are mainly used. PBF-LB/P has established itself as a method for producing mechanically resilient and geometrically complex components despite the high surface roughness known to limit its use [4]. Compared to other additive methods, the high mechanical properties and achievable component complexities are the foundation of the expansion of the application spectrum of PBF-LB/P components [4,5].

The PBF-LB/P process comprises three main steps [6]. In the first step, a powder layer is uniformly distributed across the building platform and is heated just below the melting point of the material; the powder is melted via a CO_2 laser. The building platform is then lowered by a pre-determined layer thickness, typically between 80 and 150 µm, and the process is repeated until all parts are fully generated [7]. It is worth noting that the layerwise processing employed in this technique results in the formation of unique characteristics that distinguish it from conventional manufacturing methods, such as injection molding [4].

Given the high temperatures and slow cooling rate in the PBF-LB/P process, the resulting parts exhibit a high degree of crystallinity and a homogeneous morphology [6,8]. The surface structure of the parts is primarily determined by the attachment or partial melting of powder particles, resulting in a high level of roughness [9]. However, the characteristics of parts can differ based on their location within the build chamber; these include temperature conditioning, exposure parameters, and the machine used [10,11]. This contributes to the uniqueness of the thermal history of each part in both the xy-plane and z-direction [12,13].

The exposure step is critical for the parts' properties, and requires close observation. Previous investigations have focused on temperature development during exposure, and have utilized in situ and offline methods. Lanzl et al. [14] introduced a new offline technique, the Laser-High-Speed-DSC, which analyzes maximum temperatures and heating rates for different laser parameters during exposure. Wegner et al. [15,16] examined the impact of processing parameters on the melt temperature after exposure and linked it to a viscosity model in [17]. Drummer [18] presented the resulting melt pool shape depending on energy input parameters, and correlated it to exposure temperatures measured by a pyrometer. Greiner [19] identified the scan speed as one of the most critical factors influencing exposure temperature during beam melting, and determined that a complete melting of the material could not be achieved even at a high energy density [19]. Abdelrahman and Starr [20] utilized thermal imaging for the layerwise monitoring of the PBF-LB/P process to detect any defects during laser exposure.

The manufactured parts' dimensional accuracy depends on their position and orientation, as well as the empirical corrective strategies such as adapted models, scaling parameters, or exposure parameters [21–24]. In addition, part accuracy is influenced by multiple parameters, including laser scan length, melt pool size, and exposure time and layer time variations [21,22,25,26]. The powder adhesion was quantified and found to be primarily independent of the hatch and layer count [27]. Nevertheless, the powder adhesion at the bottom tends to be higher than that found at the top of the part. The first melt depth is significantly higher than the intended depth. In addition, the layer depth depends on the hatch count [27].

Despite the benefits, it is essential to acknowledge that the PBF-LB/P process may lead to the formation of pores within the final parts. Specifically, a 3–5% porosity is typically observed for PA 12 parts, with pores mainly oriented along the layers, resulting in reduced cross-sectional areas of the parts [28]. As highlighted in prior research, this causes increased notch effects within the parts and consequently influences their mechanical properties [6,29]. Notably, the porosity within the final parts is highly dependent on the process parameters employed [30]. Further, inhomogeneous melting, mainly resulting from under-dosed energy inputs, can cause the retention of unmelted particles within the parts, as previously reported [31].

Wörz observed the influence of the energy density [32] and the hatching strategy [33] on forming part properties for tensile bars with different layer numbers in the XY orientation. An alternating hatching strategy provided the highest mechanical properties, better surface roughness, and increased dimensional stability [33]. In addition, the influence of part thickness was investigated in various studies [11,28,34]. However, no significant influence was detected for tensile bars with a 2–6 mm thickness on the main tensile properties [34]. On the other hand, part thickness in the 4–0.6 mm range exhibited distinct losses in the elastic modulus, tensile strength, and elongation at break with decreasing

wall thicknesses for all build orientations [28]. Tasch et al. [11] found distinct differences in elongation at break, with more scattering of the mechanical properties in specimens produced by P770 than in those produced by P396. Furthermore, the Poisson's ratio did not vary between thin- and thick-walled structures; therefore, structures with a thickness below 1 mm showed distinctive losses in stiffness, ultimate tensile strength, and elongation at break.

This research paper investigates the influence of part orientation, thickness, and machine on the quality and mechanical properties. In detail, the study focuses on analyzing the parts' normalized energy density, IR-thermography, porosity, surface roughness, and mechanical properties. The aim is to provide insights into the relationship between the machine used, the process parameters, and the part properties to optimize the PBF-LB/P process for thin-walled parts. The results of this study will contribute to a better understanding of the PBF-LB/P process, and enable the development of high-quality parts with improved mechanical properties.

2. Materials and Methods

This study used PA12 powder (PA 2200, EOS GmbH, Krailling, Germany) for the experiments. The powder was prepared according to the manufacturer's guidelines by blending 50% new powder with 50% used powder. The viscosity number (VN) was determined using the DIN EN ISO 307 method (VN = 66 $\pm$ 2 mL/g). The particle size distribution was obtained using a laser diffraction particle size analyzer (d10 = 39 µm, d50 = 58 µm, and d90 = 85 µm). The powder flowability was assessed using the compression depth technique developed by Hesse [35], yielding a value of 93 µm. The measurements indicated good powder and material properties.

2.1. Machines

In the present study, two industrial machines were used to conduct the experiments: an EOS Formiga P110 (P1), and an EOS P396 (P3). The Formiga P110 has a 200 $\times$ 250 $\times$ 330 mm build volume. On the other hand, the P396 is a larger machine specifically designed for handling larger lot sizes and achieving higher build rates. As a result, the P396 has a larger build volume of 350 $\times$ 350 $\times$ 600 mm. Both machines are equipped with a CO_2 laser, with the P110 laser power rated at 30 W and the P396 at 70 W. The laser focus diameter differs slightly from approx. 0.5 mm to 0.6 mm, leading to different beam offsets. Notably, the P396 offers advanced software tools, such as EOSAME, to improve the homogeneity of part properties. Apart from the differences in their build volumes, the two machines differ significantly in their design (Figure A1, Appendix A), leading to varying performance accuracy, surface finish, and dimensional stability. Both systems have controllable process- and removal-chamber heating (red features, Figure 1) to control the powder bed temperature and the temperature in the z-direction. While the P1 supplies the powder only from one side (left side), the P3 has two powder feeders to dose powder after every recoating step. The P1 adds the powder with a single blade and does not have an overflow. Therefore, the powder has to be moved after a recoating step from one side of the blade to the other. The blade of the P1 is guided over the powder bed surface in a manner analogous to a wiper on a car, which leads to different recoating speeds depending on the distance to the rotational axis. The P3 uses a double-blade cartridge and an overflow system. The double-blade system allows recoating in both directions. Compared to the P1, the P3 uses a linear movement for the recoating. After each recoating step, the blade moves a defined length over the overflow. Excessive powder falls in the overflow, guaranteeing a constant powder amount in the double-blade cartridge.

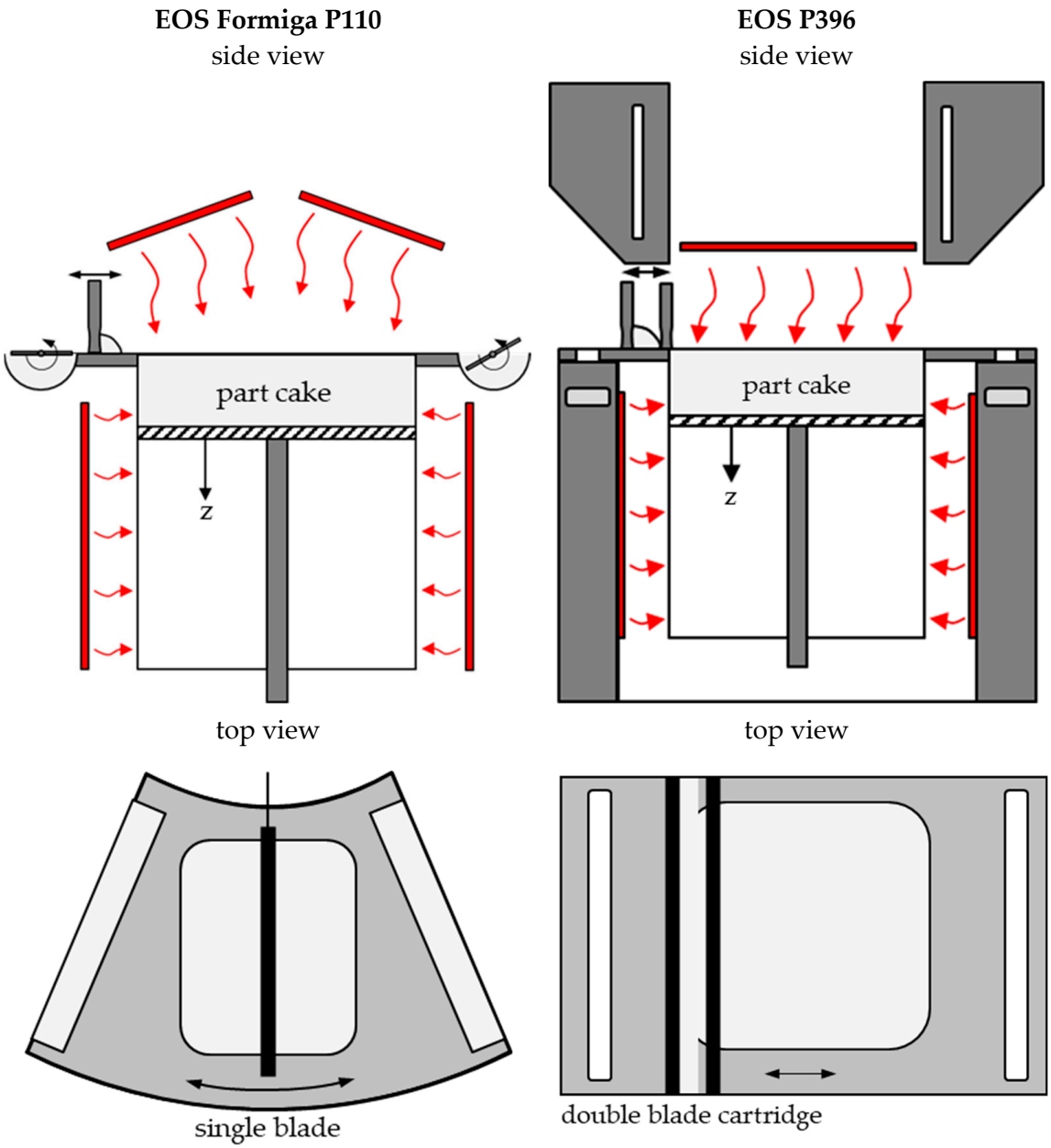

Figure 1. Machine design EOS Formiga P110 and EOS P396.

2.2. Test Specimens

Tensile bars were used to investigate the mechanical properties in relation to the wall thickness and the part position, as specified by ISO 527-2 [21]. In this study, the technical drawing for the tensile bar is presented in Figure 2. To increase the local resolution in the build chamber and the part number, the tensile bar type 1A was modified in length (1A "short"). The manufactured tensile bar is shown in Figure A2 (Appendix B). Unlike the standardized, scaled version (1BA), these shortened tensile bars were only scaled in the length direction while maintaining the same surface-to-volume ratio and cross-section within the parallel area (l1). In addition, the reduced length allowed for multiple bars to be placed next to each other to increase the resolution in the xy-plane. To understand the effect of wall thickness, the tensile bars' thicknesses were scaled according to thickness (t) in Table 1.

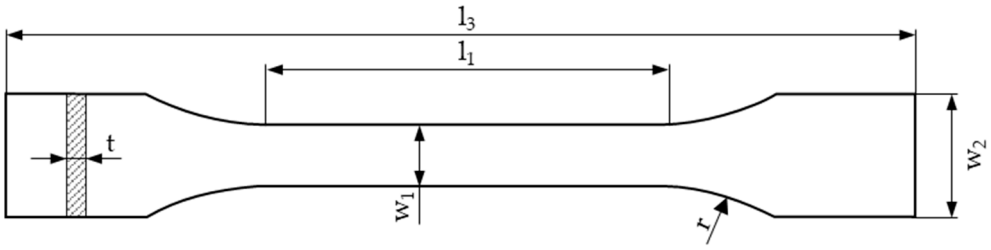

Figure 2. Tensile bar—technical drawing.

Table 1. Dimensions of the manufactured tensile bars.

Type	l_1	l_3	w_1	w_2	r	t
1 A "short"	40 mm	90 mm	10 mm	20 mm	12 mm	0.5; 1; 1.5; 2; 3; 4 mm

2.3. Build Job Layouts

A similar layout for the build job was developed for both machines to compare the two machine sizes (Figure 3). In total, three main part orientations were built: XY, XZ, and Z orientations. Due to the hatch grid that was pre-defined by the hatch distance, all parts were placed to contain the maximum number of hatch lines possible for the given part thickness [11]. This affected the XZ- and Z-oriented parts.

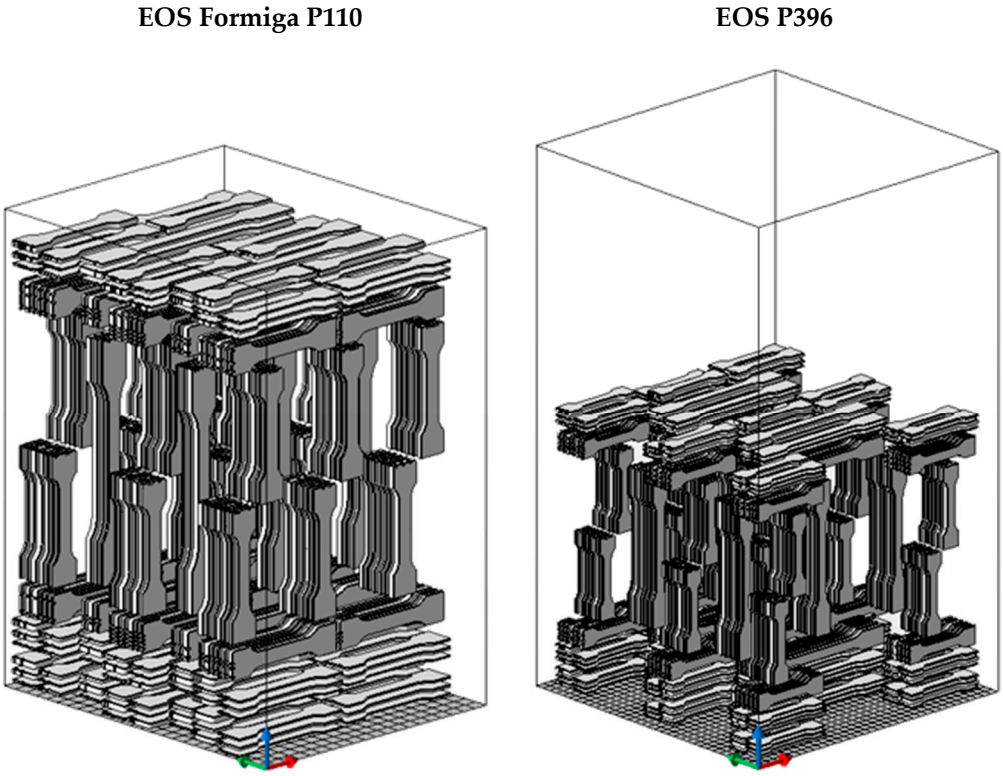

Figure 3. Build job layouts for the P1 and P3.

2.4. Process Parameters

The scaling parameters for the used powder and the machines were determined based on the manufacturer's guidelines. The z-compensation was selected for a single layer. Subsequently, the EOS exposure parameters for the system, powder material, and layer thickness were used accordingly. The scaling and processing parameters employed are listed in Table 2.

Table 2. Scaling and processing parameters.

Type	Unit	Formiga P110	P396
x-Scaling	%	3.02	2.8
y-Scaling	%	2.97	3.0
z-Scaling	%	z(0) 2.6–z(300) 2.0	z(0) 2.55–z(300) 1.4
z-Compensation	µm	100	120
Layer thickness	µm	100	120
Build height	mm	310	310
Beam offset	mm	0.21	0.3
Process-chamber temperature	°C	169	174
Removal-chamber temperature	°C	150	130
Exposure parameters		PA2200_100_102	PA2200_120_111

After printing, the parts were carefully cleaned with a brush, and post-processed via glass bead blasting. For the blast process, a Wiwox DI 12 machine was used for 3 min with a blasting pressure of 3 bar and glass beads between 100 and 200 um. After cleaning, the parts were immediately stored in a vacuum to maintain the dry conditioning for mechanical testing.

2.5. Analysis Methods

2.5.1. Normalized Energy Density (NED)

The energy density (*ED*), expressed in J/mm^2, is a crucial factor in the melting process, and significantly influences both the porosity and mechanical properties; however, it represents a steady state due to the overlapping of the scan vectors defined by the hatch distance [36]. The *ED* differs significantly from the real energy input for thin parts and small melt pools, containing only few scan vectors. As proposed in [28], the *ED* was calculated for each layer, part orientation, and cross-section according to Equation (1).

$$ED = \frac{1}{A}\sum_{i=1}^{n} P_i \frac{s_i}{v_i} \quad (1)$$

The total energy supplied by the three scan types—contour, hatch, and edge scan—was calculated by Equation (1). For each scan type, the calculation accounted for the laser power (P_i) in W, path lengths (s_i) in mm, and velocities (v_i) in mm/s. The sum of these values was then divided by the section area (A) in mm^2. For comparison, the *ED* was normalized by the calculated *ED* of the XY-oriented tensile bar leading to the NED of the system.

2.5.2. Thermographic Measurements

An infrared (IR) thermographic system, Velox 1310 k SM (IRCAM GmbH, Erlangen, Germany), was utilized to characterize the exposure process. This system operates in short and medium-wavelength ranges between 1.5 and 5.5 µm, and uses a sapphire glass window to protect the detector from damage. The transmission of sapphire glass drops was close to 0 for radiation of wavelengths above 6 µm to filter out the wavelength of the CO_2-laser (λ_{CO2} = 10.6 µm). The integration time was set to 25 µs. For all experiments, a simplified assumption was made to keep the emission coefficient constant and adapt according to the initial temperature of the build chamber; this was measured by the system's pyrometer. As optical properties were temperature-dependent and changed during the phase transition from a solid to a viscous state, the temperature values shown could not be understood as absolute values, but the shown influences were interpreted parametrically.

2.5.3. Geometry

The thickness and width of the tensile bars were measured by a micrometer at three points. Further, the parts were scanned by a flatbed scanner. The scanning resolution was

set to 1200 dpi, leading to a pixel size of ~21 µm. Due to the instability of the 0.5 mm thin parts, the width was measured optically. Additionally, the surface area of the tensile bars was calculated.

2.5.4. Surface Roughness

A 3D-scanner Comet L3D 2 equipped with a C45 objective lens from Carl Zeiss AG was used to measure the surface roughness. The 3D-scanner captured high-resolution 3D scans of the primary surface, which were then processed using MountainsLab 9.1 software from Digital Surf. A parallel tensile bar area of 9 mm × 50 mm was evaluated. A second polynomial approach was used to remove the form. The surface was characterized by the arithmetical mean height (S_a).

2.5.5. Part Density and Porosity

A volumetric approach was used to calculate the part density. The cross-section area and the thickness calculated the volume. The weight was measured with a precision scale. Further, the inner porosity was analyzed using computed tomography with a voxel size of 8 µm × 8 µm × 8 µm.

2.5.6. Mechanical Properties

Mechanical testing was performed according to DIN EN ISO 527-1 [17] and -2 [18]. A tensile testing machine of Type 1484 (Zwick Roell, Ulm, Germany) with an extensometer was used. The testing parameters were adapted to the length of the tensile bar to achieve a comparable strain rate. The E-modulus was measured with a testing speed of 0.5 mm/min. The elongation at break was measured at 25 mm/min. The clamping length was set to 62 mm. Further, mechanical testing was observed with an infrared thermographic system, Infratec Vario Cam HD.

3. Results

3.1. Normalized Energy Density

The influence of part orientation and thickness is crucial on the melt pool size, affecting the energy input. Figure 4a presents the manufactured parts' calculated normalized energy density (NED). A notable increase in NED was observed for the P1 system as the part thickness decreased, while a decrease in NED was identified for the P3 system. This finding reveals a significant dependency on the machine and exposure strategy employed.

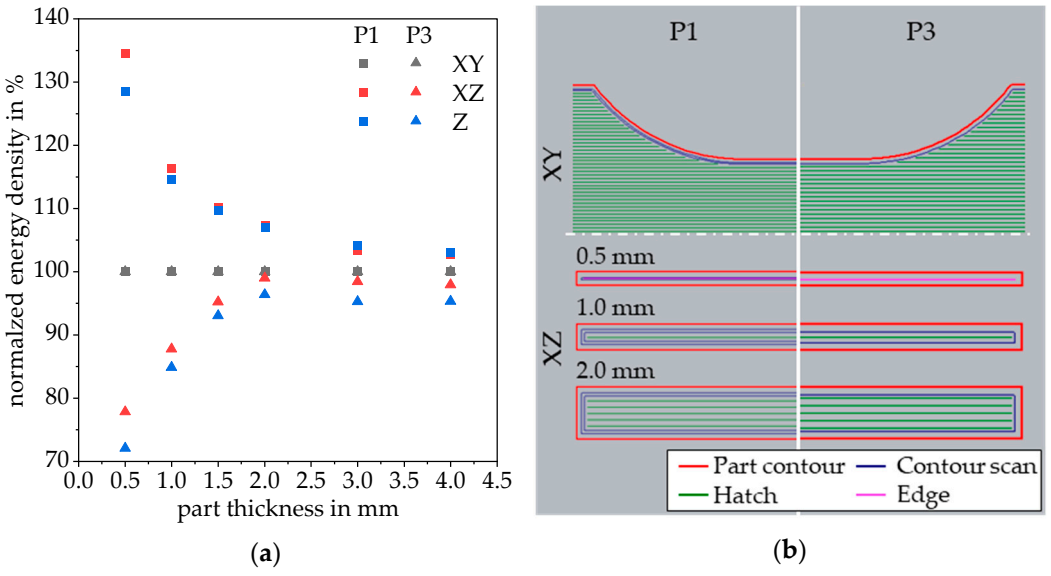

Figure 4. Calculated normalized energy density dependent on the part thickness (**a**); scan pattern of a scan in the x-direction for XY- and XY-oriented parts (**b**).

The exposure strategies were optimized for the laser focus diameter and the used layer thickness of the systems. Figure 4b provides a representative illustration of the exposure strategies for both XY and XZ orientations. The XZ-oriented parts demonstrated the same scan pattern as the Z-oriented parts. However, while the P1 system incorporated a pre- and post-contour scan, the P3 system employed only a post-contour scan. Further, the hatch distance and beam offsets differed due to different laser focus diameters. The difference in contour scans substantially affected the 0.5 mm part. While the P1 system used an edge and a contour scan, the P3 system relied solely on an edge exposure, leading to a decreased energy input.

Table 3 presents a comprehensive overview of the number of contour scans and hatch scans employed for each thickness in the XZ and Z orientation. These differences in scan vector number can significantly impact the temperatures during exposure, and affect the part properties. In addition to the scanning strategy, ref. [19] demonstrated that scan vector length and laser return time play a vital role in temperature development. The alternating scanning strategy causes the scanning direction to change with every layer, alternating in x- and y-directions; this leads to long and short scan vectors. Table 3 presents the aspect ratio between these vector lengths for XZ and Z orientations, depending on part thickness.

Table 3. Scan pattern in the x-direction for xz- and z-oriented parts depending on the part thickness and the machine used, and aspect-ratio of the scan path length in x- and y-direction.

Thickness	Contour	P1 Hatch	Edge	Contour	P3 Hatch	Edge	Aspect-Ratio xy	xz	z
0.5 mm	1	-	1	-	-	1	9	0	0
1.0 mm	2	1	-	1	1	-	9	607	63
1.5 mm	2	3	-	1	3	-	9	136	14
2.0 mm	2	5	-	1	5	-	9	76	8
3.0 mm	2	9	-	1	7	-	9	41	4
4.0 mm	2	13	-	1	11	-	9	28	3

The 0.5 mm part was close to the resolution limit of the machines due to the laser focus diameter. Therefore, both machines used an edge scanning parameter containing one single scan vector. No change in scanning direction was possible for this part thickness, leading to an aspect ratio of zero (Figure 4b). The highest aspect ratio was calculated for the 1.0 mm part, attributable to the short scan vectors perpendicular to part thickness (<1 mm). The aspect ratio diminished with increasing part thickness, as the scan vector length perpendicular to the part thickness expanded. In the XZ orientation, the longest scan vector was defined by the part length, and measured approximately 90 mm, while it was only 10 mm for the z-oriented parts (width of the tensile bar). These differences in scan vector length led to different laser return times, and an influence for the exposure temperatures.

3.2. IR-Thermography

The melting process is affected by various factors, including laser power, scan speed, hatch distance, and laser return time [19]. The maximum temperature is mainly concentrated near the laser focus diameter, and increases due to overlapping with previously melted areas [19]. Therefore, the highest temperatures can occur near the turnaround points of the laser or other points with a low laser return time. Figure 5a shows that most of the measured maximum temperatures fell within a range of 20 °C between 215 °C and 235 °C, which was sufficient for melting the polymer and is comparable to other studies [19,37]. Moreover, the maximum temperature for XY-oriented parts was not dependent on the machine used or the part's thickness. Noticeably, parts in Z orientation using the P1 system showed a significantly higher maximum temperature. The short scan vectors/aspect-ratio led to shorter laser return times. Further, the used pre-contour added additional energy to the system. As a result, the melt had less time to cool down before the laser heated the same area again, yielding a higher temperature. Furthermore, a decrease in the maximum

peak temperature was observed in parts using the edge parameter (0.5 mm in XZ and Z orientation). The maximum temperature dropped when using different laser power and scan speed settings. The edge parameters were used in areas smaller than the machine's resolution limit. Therefore, this parameter was a tradeoff between the geometric accuracy and the existence of a small feature.

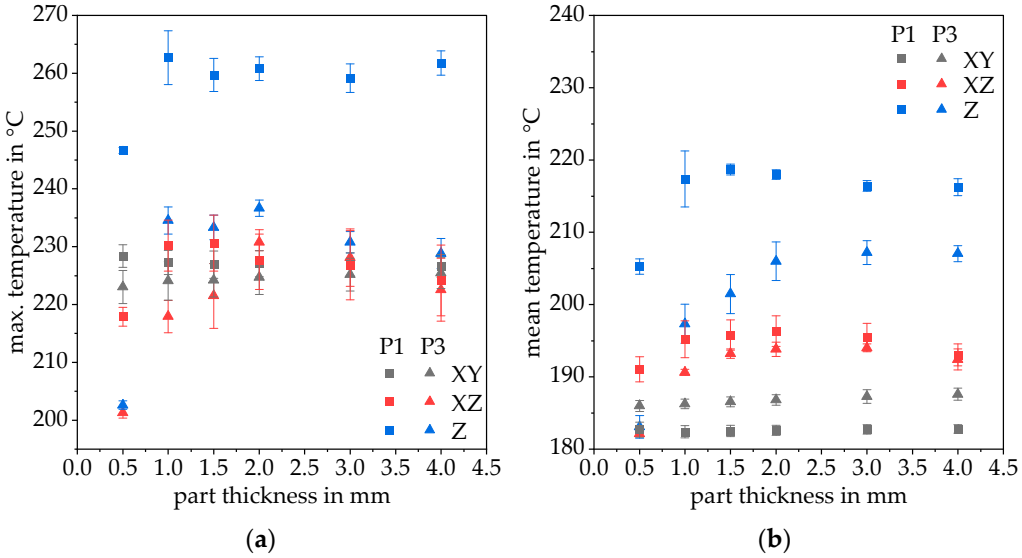

Figure 5. Peak temperature of the mean temperature profile (**a**) and peak temperature of the maximum temperature profile (**b**) depending on the part thickness and orientation.

While the maximum temperature provides critical insights into the melting process, the mean temperature offers information on the entire melt pool. Figure 5b revealed that Z-oriented parts had the highest mean temperatures, while XY-oriented parts had the lowest. This is because the Z-orientation had the smallest melt pool size and the shortest exposure time. Due to the short exposure time, the melt pool had no time to cool down during exposure, resulting in a higher mean temperature. Conversely, the exposed part could dissipate heat into the powder bed and processing chamber for XY-orientation, resulting in a temperature profile over the melt pool and a lower mean temperature. The impact of part thickness on the mean temperature was minimal for XY- and XZ-oriented parts. However, the P3 system exhibited a drop in the mean temperature for parts thinner than 2 mm for Z-oriented parts. The pre-contour used in the P1 system compensated for the decrease compared to the P3 system. Overall, a drop in temperature for the smallest parts in XZ- and Z-orientation was observed due to the edge parameters used.

3.3. Porosity and Surface Roughness

The surface roughness and the part density are important part characteristics influenced by the process parameters and part orientation. The surface roughness is caused partly by molten particles that adhere to the surface. These particles can be partially removed by blasting. The blasting process smooths the peak heights of the surface, but the peak depths are mainly unaffected.

Figure 6a shows that the surface roughness was independent of the machine used, even though the P3 used a layer thickness of 120 µm, compared to the P1 system using 100 µm. The surface roughness remained relatively constant between part thicknesses of 1–4 mm, but slightly increased for a part thickness of 0.5 mm. The orientation showed the most significant influence on surface roughness, with the XY orientation resulting in the lowest surface roughness. On the other hand, the XZ and Z orientations showed the highest surface roughness because the build-up direction and the layer-by-layer process affected the measured surface. The effects mentioned are consistent with the current state-of-the-art [30,38].

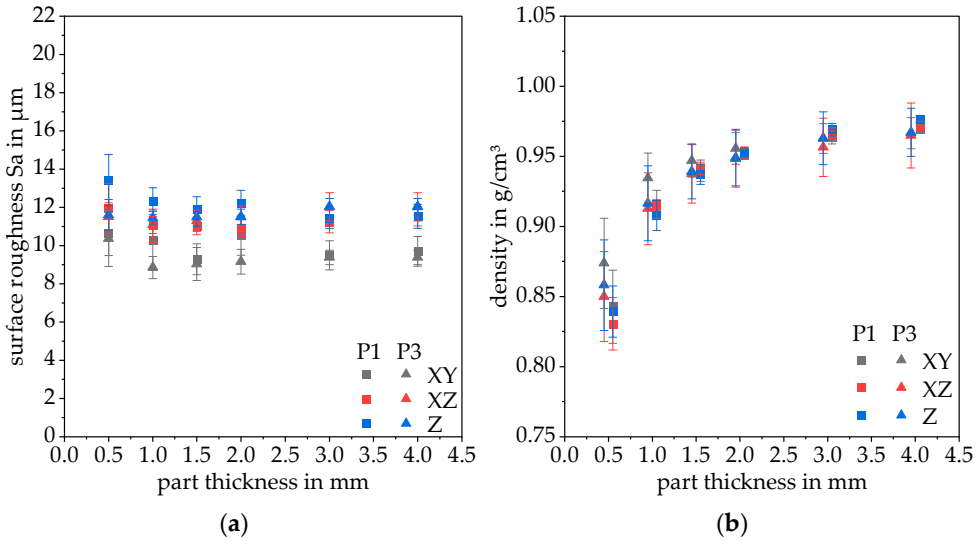

Figure 6. Surface roughness S_a (**a**) and part density (**b**) depending on the part thickness, orientation, and machine used.

Figure 6b illustrates the dependence of part density on the part thickness, part orientation, and the type of machine. The density measurement is based on a volumetric approach, meaning that surface and geometrical deviations can affect the measurement. The part density is observed to be independent of the machine used, but the standard deviation of measured values is larger for the P3 machine than the P1 machine. This suggests that other factors, such as the powder quality and process parameters, may have a greater influence on the part density. Additionally, the machine design can influence the part density. Due to the powder recoating system of the P1, the recoating speed differed locally in the y-direction. Greiner et al. [39] showed that the recoating speed affects the powder bed surface and the part density. Further, because of the one-sided feeding system of the P1, the powder temperature differed significantly depending on the recoating direction (up to 20 °C). Hesse et al. [35] measured a significant change in powder flowability depending on the powder temperature. Both can influence the part density, leading to the increased standard deviation for the P1 system. However, the density dropped significantly for parts thinner than 2 mm for both machines. This was likely due to the increased influence of surface roughness on the part density. The surface roughness creates an "outer porosity" which can significantly affect the volume measurement of the part [28]. Therefore, the surface roughness must be carefully considered in part design and behavior, particularly for thin structures.

Figure 7a depicts the inner porosity for 1 and 2 mm thick parts in the XZ- and Z-orientation. It is noted that the inner porosity increased with increasing wall thickness. This effect was also observed by Sindinger et al. [28]. The inner porosity is primarily independent of the machine used. Pores in the part act as imperfections and can initiate cracks. Once a crack is initiated, it propagates in the stress plane until it reaches a surface, leading to part failure. Pores are created by air volume in the powder bed due to the bulk density of the used powder system. For PA 12, the bulk density was 0.45 g/cm^3 compared to the compact material density of 1.01 g/cm^3. By melting the powder, the particles combined their coalescent behaviors influenced by the material system and the molecular weight. As a result, the trapped air created pores in the melt pool. Wudy [40] showed that pores are stationary for PA12, and that pore removal is a function of time and temperature. The polymer melt can dissolve the trapped air due to diffusion processes. Stichel et al. [29] calculated the critical pore diameter, and concluded that pore diameter is not critical for crack initiation. Overall, pores lead to a measurement error for the cross-section, and influence the calculation for normalized mechanical properties as an error. Figure 7b presents exemplary cross-sections for the P1 and P3 machines for XZ- and

Z orientations with part thicknesses of 1.0 and 2.0 mm. No difference in pore shape or distribution was observed between the machines and orientations.

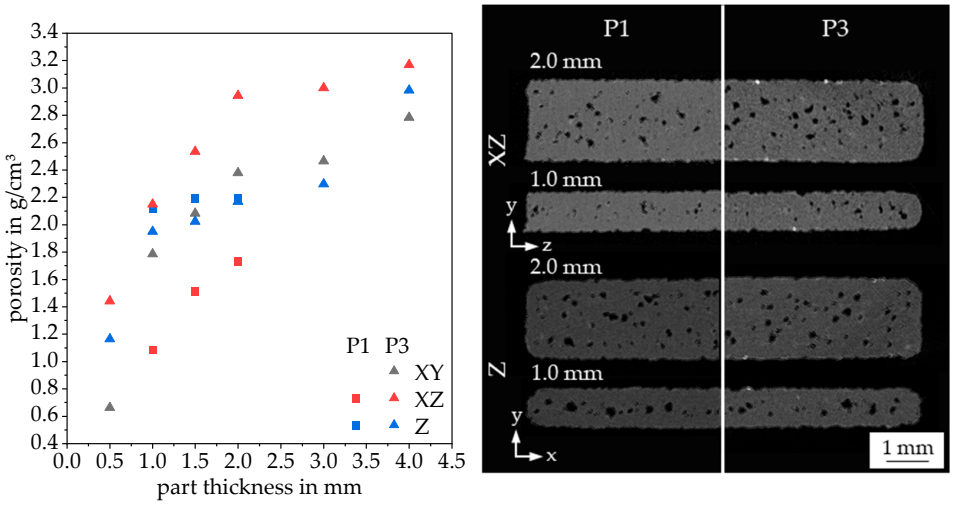

(**a**) (**b**)

Figure 7. CT-measured porosity related to the part thickness and orientation (**a**); exemplary section of the pore form and distribution for xz- and z-oriented parts (**b**).

3.4. Mechanical Properties

Figure 8a illustrates the tested specimens' measured E-modulus. The parts manufactured with the P1 system showed a slightly lower E-modulus and higher standard deviation than those built with the P3 system. There was a decrease in E-modulus for parts thinner than 2 mm. The E-modulus is a standardized characteristic that depends on the cross-section of the tensile bar. Measurement errors due to surface roughness and porosity can affect E-modulus measurement, and may increase with decreasing part thickness due to a higher surface-to-volume ratio.

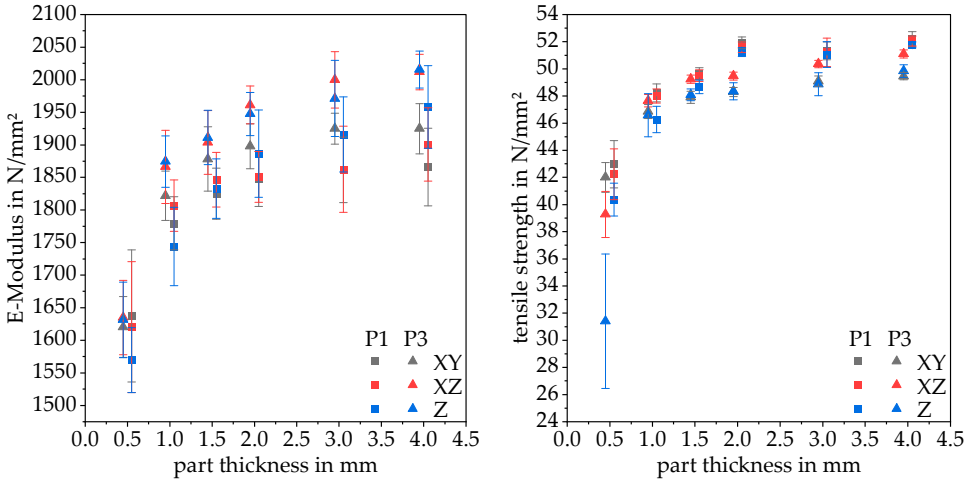

(**a**) (**b**)

Figure 8. E-Modulus (**a**) and tensile strength (**b**) depending on the part thickness, machine, and orientation.

Figure 8b shows the specimens' ultimate tensile strength (UTS). As the P3 reached a slightly higher UTS than P1, there was no significant difference between the orientations. The UTS dropped for specimens thinner than 1.5 mm. The 0.5 mm, Z-oriented parts manufactured on the P3 machine showed the lowest value and a large standard deviation. Figure 9a depicts the elongation at break of the tested specimens. The most significant

difference was observed in the Z orientation, where parts manufactured on the P1 system were comparable to XY and XZ orientation. However, parts manufactured on the P3 system showed a significant decrease in elongation at break. While the density and surface roughness were mostly independent of the used system, the most significant difference was identified in the maximum and the mean temperatures of the Z-oriented parts during exposure. This could influence the breaking behavior and lead to the results shown in Figure 9a. The overall elongation at break decreased for parts thinner than 1.5 mm, comparable to the ultimate strength. Figure 9b shows the stress–strain curve for exemplary samples manufactured on the P1 and P3 systems. No significant necking of the parts was observed, indicating a brittle breaking behavior.

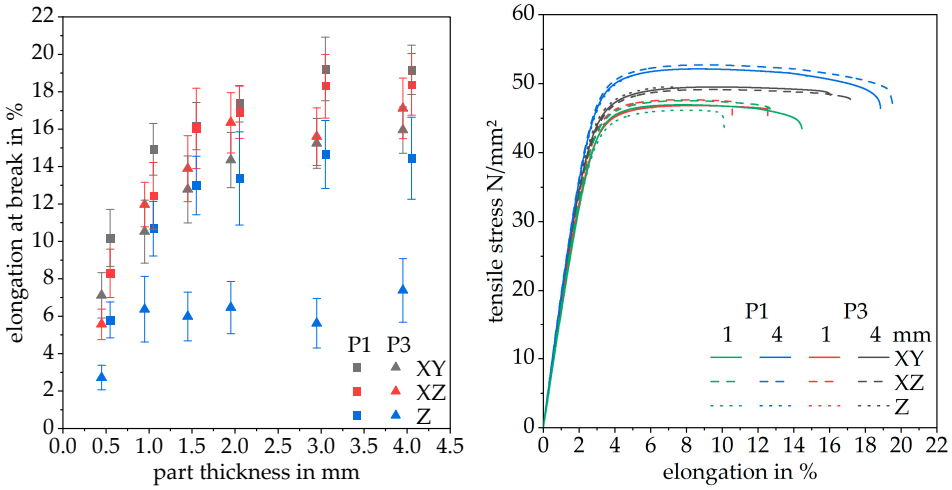

(**a**) (**b**)

Figure 9. Elongation at break (**a**) and stress-elongation behavior (**b**) depending on the part thickness, machine, and orientation.

During the loading process, most mechanical energy, excluding the elastic energy, is dissipated into thermal energy. In addition, imperfections such as surface roughness or pores can act as crack initiators. As a result, the local stress will increase at these defects, and an increased temperature can be observed. Figure 10a compares the influence of the part thickness (XY-orientation, P1 system). With decreasing wall thickness, the temperature at the crack initiation decreased. A reason for this behavior was the reduction in the deformation and a therefore a decrease in mechanical energy, which was dissipated into thermal energy.

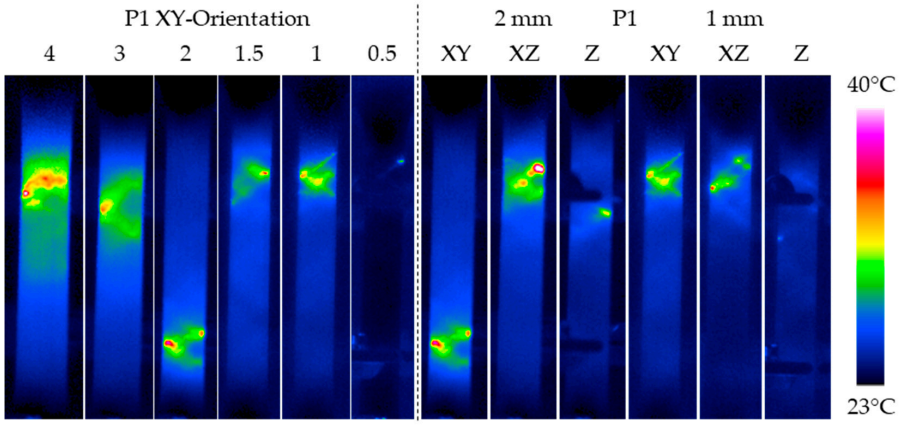

(**a**) (**b**)

Figure 10. Thermography of the tensile testing, 1 frame before break: influence of the part thickness on the breaking behavior (**a**); influence of the part orientation (**b**).

All parts exhibited brittle breaking behavior with the crack initiation at the short edge of the tensile bar. The crack initiated on the tensile bar's side, and shifted the force's path off-center. The part showed an abrupt failure behavior once the crack reached a critical length. Due to the off-center shift of the force curve, momentum was created, leading to the V-shaped breaking of the tensile bar. At the crack tip, the force paths for the 3 mm and 2 mm thick parts which formed a V-shape were seen. The thinnest part showed little to no increase in the temperature due to low deformation levels. Surface defects can speed up the failure of the part while testing. Figure 10b shows the influence of the part orientation for two chosen wall thicknesses. For Z-oriented parts, the crack initiation was less visible.

4. Conclusions

This study has demonstrated the significant influence of part orientation, thickness, and machine type on the normalized energy density (NED), surface roughness, porosity, and mechanical properties of thin-walled parts. The key findings and their interrelations are summarized as follows:

1. Normalized Energy Density (NED): NED was found to be highly dependent on the exposure strategy employed. For the P1 system, NED increased as the part thickness decreased, while the P3 system showed a decrease in NED for the EOS parameters. The differences in contour scans significantly impacted the exposure temperatures and part properties. This highlights the importance of understanding the machine-specific parameters and exposure strategies when designing and fabricating additively manufactured parts.
2. Surface Roughness: Surface roughness was largely independent of the machine used, and remained relatively constant between part thicknesses of 1–4 mm. However, the orientation had the most significant influence on surface roughness, with XY-orientation resulting in the lowest surface roughness and XZ- and Z-orientations showing the highest surface roughness. This indicates that optimizing part orientation is a key factor in improving surface quality.
3. Porosity: Inner porosity increased with increasing wall thickness, and was primarily independent of the machine used. Pores in the part act as imperfections, initiating cracks and affecting the mechanical properties. Therefore, careful consideration of part thickness is crucial when designing and fabricating parts for applications where high strength and minimal porosity are required.
4. Mechanical Properties: The E-modulus and ultimate tensile strength (UTS) were found to decrease for parts thinner than 2 mm, while elongation at break decreased for parts thinner than 1.5 mm. The P3 system reached a slightly higher UTS than the P1 system, but the differences were not significant. The most significant difference in elongation at break was observed in the Z-orientation, suggesting the impact of machine type and orientation on the mechanical performance of parts.

This study emphasized the importance of optimizing machine-specific parameters, part orientation, and thickness to achieve desired part properties in additive manufacturing processes. By understanding these factors and their interdependencies, it is possible to improve the quality, performance, and reliability of additively manufactured parts for various applications. Future research should continue to explore the effects of these variables and other process parameters on the properties of additively manufactured parts to develop more comprehensive guidelines and design rules for the industry.

Author Contributions: A.J.: Conceptualization, Data curation, Formal analysis, Investigation, Methodology, Project administration, Visualization, Writing—original draft, Writing—review and editing; S.C.: Methodology, Investigation, Validation, Data curation, Formal analysis, Visualization, Writing—review and editing; D.D.: Resources, Supervision, Funding acquisition, Writing—review and editing. All authors have read and agreed to the published version of the manuscript.

Funding: This research was funded by the Deutsche Forschungsgemeinschaft (DFG, German Research Foundation) within CRC 814 "Additive Manufacturing" (Project-ID 61375930) Subproject T3 and A3.

Data Availability Statement: The data supporting this study's findings are available from the corresponding author upon reasonable request.

Acknowledgments: We gratefully acknowledge financial support from the Deutsche Forschungsgemeinschaft and Friedrich-Alexander-Universität Erlangen-Nürnberg within the funding program "Open Access Publication Funding".

Conflicts of Interest: The authors declare that they have no known competing financial interests or personal relationships that could have appeared to influence the work reported in this paper.

Appendix A

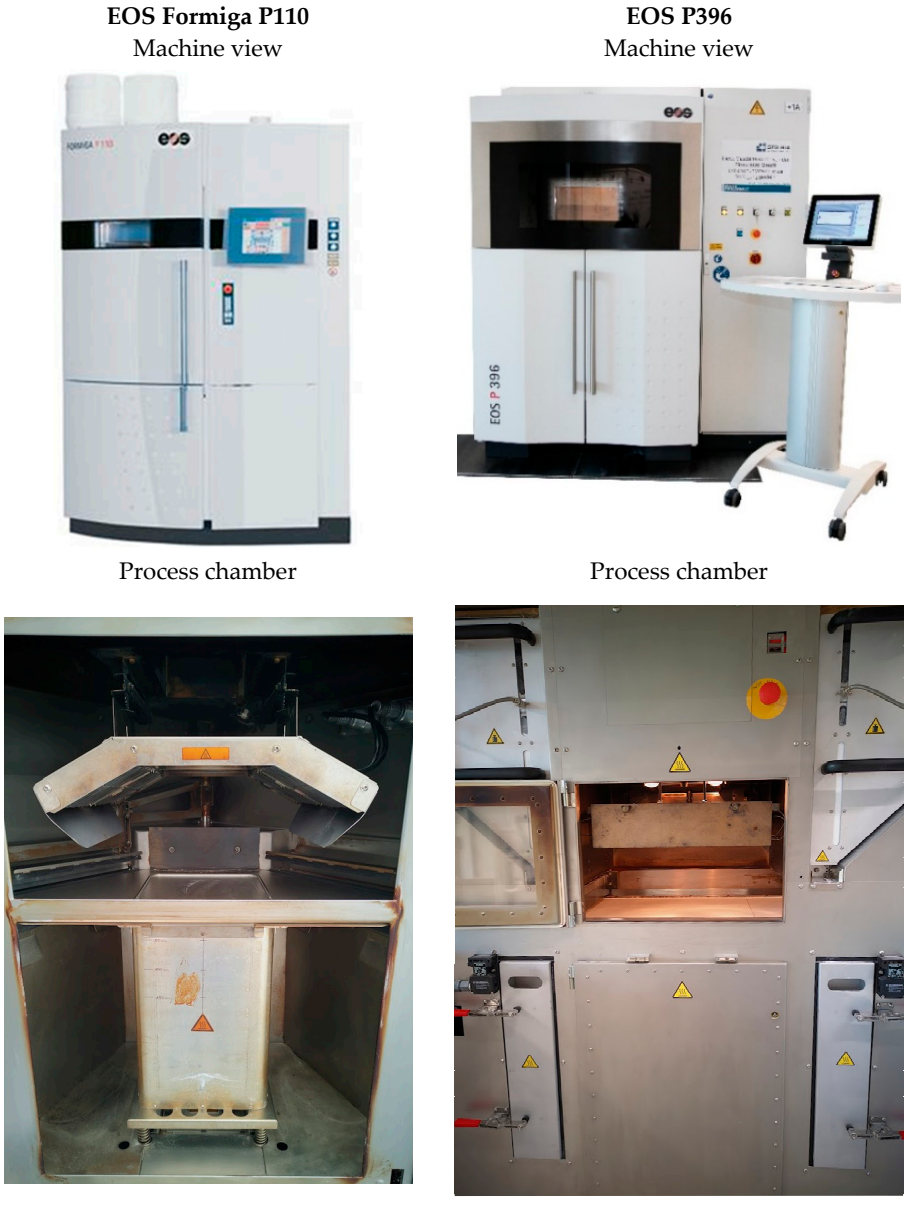

Figure A1. Machine overview and process chamber.

Appendix B

Figure A2. Manufactured tensile bar.

References

1. Mehrpouya, M.; Dehghanghadikolaei, A.; Fotovvati, B.; Vosooghnia, A.; Emamian, S.S.; Gisario, A. The Potential of Additive Manufacturing in the Smart Factory Industrial 4.0: A Review. *Appl. Sci.* **2019**, *9*, 3865. [CrossRef]
2. Tofail, S.A.M.; Koumoulos, E.P.; Bandyopadhyay, A.; Bose, S.; O'Donoghue, L.; Charitidis, C. Additive manufacturing: Scientific and technological challenges, market uptake and opportunities. *Mater. Today* **2018**, *21*, 22–37. [CrossRef]
3. Ligon, S.C.; Liska, R.; Stampfl, J.; Gurr, M.; Mülhaupt, R. Polymers for 3D Printing and Customized Additive Manufacturing. *Chem. Rev.* **2017**, *117*, 10212–10290. [CrossRef]
4. Wörz, A.; Wudy, K.; Drummer, D.; Wegner, A.; Witt, G. Comparison of long-term properties of laser sintered and injection molded polyamide 12 parts. *J. Polym. Eng.* **2018**, *38*, 573–582. [CrossRef]
5. Vanaei, H.R.; El Magri, A.; Rastak, M.A.; Vanaei, S.; Vaudreuil, S.; Tcharkhtchi, A. Numerical–Experimental Analysis toward the Strain Rate Sensitivity of 3D-Printed Nylon Reinforced by Short Carbon Fiber. *Materials* **2022**, *15*, 8722. [CrossRef] [PubMed]
6. Schmid, M. *Laser Sintering with Plastics: Technology, Processes, and Materials*, 1st ed.; Hanser Publications, Cincinnati: Munich, Germany, 2018.
7. Goodridge, R.D.; Tuck, C.J.; Hague, R.J.M. Laser sintering of polyamides and other polymers. *Prog. Mater. Sci.* **2012**, *57*, 229–267. [CrossRef]
8. Greiner, S.; Jaksch, A.; Cholewa, S.; Drummer, D. Development of material-adapted processing strategies for laser sintering of polyamide 12. *Adv. Ind. Eng. Polym. Res.* **2021**, *4*, 251–263. [CrossRef]
9. Launhardt, M.; Wörz, A.; Loderer, A.; Laumer, T.; Drummer, D.; Hausotte, T.; Schmidt, M. Detecting surface roughness on SLS parts with various measuring techniques. *Polym. Test.* **2016**, *53*, 217–226. [CrossRef]
10. Rietzel, D.; Drexler, M.; Kühnlein, F.; Drummer, D. Influence of temperature fields on the processing of polymer powders by means of laser and mask sintering technology. In Proceedings of the 2011 International Solid Freeform Fabrication Symposium, Austin, TX, USA, 8–10 August 2011; University of Texas at Austin (Freeform): Austin, TX, USA, 2011; pp. 252–254.
11. Tasch, D.; Mad, A.; Stadlbauer, R.; Schagerl, M. Thickness dependency of mechanical properties of laser-sintered polyamide lightweight structures. *Addit. Manuf.* **2018**, *23*, 25–33. [CrossRef]
12. Josupeit, S.; Schmid, H.-J. Temperature history within laser sintered part cakes and its influence on process quality. *Rapid Prototyp. J.* **2016**, *22*, 788–793. [CrossRef]
13. Josupeit, S.; Schmid, H.-J. Three-Dimensional In-Process Temperature Measurement of Laser Sintered Part Cakes. In Proceedings of the 2014 International Solid Freeform Fabrication Symposium, Austin, TX, USA, 4–6 August 2014; University of Texas at Austin: Austin, TX, USA, 2014. [CrossRef]
14. Lanzl, L.; Wudy, K.; Drexler, M.; Drummer, D. Laser-high-speed-DSC: Process-oriented Thermal Analysis of PA 12 in Selective Laser Sintering. *Phys. Procedia* **2016**, *83*, 981–990. [CrossRef]
15. Wegner, A.; Witt, G. Process Monitoring in Laser Sintering Using Thermal Imaging. In Proceedings of the 2011 International Solid Freeform Fabrication Symposium, Austin, TX, USA, 8–10 August 2011; University of Texas at Austin: Austin, TX, USA, 2011. [CrossRef]
16. Wegner, A.; Witt, G. Understanding the decisive thermal processes in laser sintering of polyamide 12. In *AIP Conference Proceedings*; AIP Publishing LLC: Cleveland, OH, USA, 2015; p. 160004. [CrossRef]
17. Mielicki, C.; Wegner, A.; Gronhoff, B.; Wortberg, J.; Witt, G. Prediction of PA12 melt viscosity in laser sintering by a time and temperature dependent rheological model. *RTejournal* **2012**, *32*, 1–32.
18. Drummer, D.; Drexler, M.; Wudy, K. Resulting melt-pool-shape during selective beam melting of thermoplastics as function of energy input parameters. In Proceedings of the DDMC 2014, Fraunhofer Direct Digital Manufacturing Conference, Berlin, Germany, 12–13 March 2014; Fraunhofer Verlag: Aachen, Germany, 2014.
19. Greiner, S.; Wudy, K.; Wörz, A.; Drummer, D. Thermographic investigation of laser-induced temperature fields in selective laser beam melting of polymers. *Opt. Laser Technol.* **2019**, *109*, 569–576. [CrossRef]

20. Abdelrahman, M.; Starr, T.L. Layerwise Monitoring of Polymer Laser Sintering Using Thermal Imaging. In Proceedings of the 2014 International Solid Freeform Fabrication Symposium, Austin, TX, USA, 4–6 August 2014; University of Texas at Austin: Austin, TX, USA, 2014. [CrossRef]
21. Launhardt, M.; Fischer, C.; Drummer, D. Research on the Influence of Geometry and Positioning on Laser Sintered Parts. *Appl. Mech. Mater.* **2015**, *805*, 105–114. [CrossRef]
22. Raghunath, N.; Pandey, P.M. Improving accuracy through shrinkage modelling by using Taguchi method in selective laser sintering. *Int. J. Mach. Tools Manuf.* **2007**, *47*, 985–995. [CrossRef]
23. Soe, S.P. Quantitative analysis on SLS part curling using EOS P700 machine. *J. Mater. Process. Technol.* **2012**, *212*, 2433–2442. [CrossRef]
24. Wang, R.-J.; Wang, L.; Zhao, L.; Liu, Z. Influence of process parameters on part shrinkage in SLS. *Int. J. Adv. Manuf. Technol.* **2007**, *33*, 498–504. [CrossRef]
25. Drexler, M. Zum Laserstrahlschmelzen von Polyamid 12: Analyse Zeitabhängiger Einflüsse in der Prozessführung. Ph.D. Thesis, Lehrstuhl für Kunststofftechnik, Erlangen, Germany, 2016.
26. Deng, X.; Zong, G.; Beaman, J.J. Parametric Analysis for Selective Laser Sintering of a Sample Polymer System. In Proceedings of the 1992 International Solid Freeform Fabrication Symposium, Austin, TX, USA, 3–5 August 1992.
27. Launhardt, M.; Drummer, D. Determination of the fundamental dimension development in building direction for laser-sintered parts. *J. Polym. Eng.* **2019**, *39*, 197–206. [CrossRef]
28. Sindinger, S.-L.; Kralovec, C.; Tasch, D.; Schagerl, M. Thickness dependent anisotropy of mechanical properties and inhomogeneous porosity characteristics in laser-sintered polyamide 12 specimens. *Addit. Manuf.* **2020**, *33*, 101141. [CrossRef]
29. Stichel, T.; Frick, T.; Laumer, T.; Tenner, F.; Hausotte, T.; Merklein, M.; Schmidt, M. A Round Robin study for Selective Laser Sintering of polyamide 12: Microstructural origin of the mechanical properties. *Opt. Laser Technol.* **2016**, *89*, 31–40. [CrossRef]
30. Wegner, A. Theorie Über die Fortführung von Aufschmelzvorgängen als Grundvoraussetzung für eine Robuste Prozessführung Beim Laser-Sintern von Thermoplasten. Ph.D. Thesis, Universitätsbibliothek Duisburg-Essen, Essen, Germany, 2015.
31. Zarringhalam, H. Investigation into Crystallinity and Degree of Particle Melt in Selective Laser Sintering, Loughborough University. 2007. Available online: https://repository.lboro.ac.uk/articles/Investigation_into_crystallinity_and_degree_of_particle_melt_in_selective_laser_sintering/9516743 (accessed on 2 June 2020).
32. Wörz, A.; Wudy, K.; Drummer, D. Understanding the influence of energy-density on the layer dependent part properties in laser-sintering of PA12. In Proceedings of the Annual International Solid Freeform Fabrication Symposium, Austin, TX, USA, 12–14 August 2019; pp. 1560–1569.
33. Wörz, A.; Drummer, D. Understanding hatch-dependent part properties in SLS. In Proceedings of the 2018 International Solid Freeform Fabrication Symposium, Austin, TX, USA, 13–15 August 2018; pp. 1360–1369.
34. Majewski, C.; Hopkinson, N. Effect of section thickness and build orientation on tensile properties and material characteristics of laser sintered nylon-12 parts. *Rapid Prototyp. J.* **2011**, *17*, 176–180. [CrossRef]
35. Hesse, N.; Winzer, B.; Peukert, W.; Schmidt, J. Towards a generally applicable methodology for the characterization of particle properties relevant to processing in powder bed fusion of polymers—From single particle to bulk solid behavior. *Addit. Manuf.* **2021**, *41*, 101957. [CrossRef]
36. Launhardt, M. *Zur Entstehung von Dimensionen und Maßabweichungen beim Laserstrahlschmelzen von Kunststoffen*; FAU University Press: Erlangen, Germany, 2021.
37. Cholewa, S.; Jaksch, A.; Drummer, D. Coalescence Behavior of Polyamide 12 as Function of Zero-Shear Viscosity and Influence on Mechanical Performance. In Proceedings of the 2022 International Solid Freeform Fabrication Symposium, Austin, TX, USA, 25–27 July 2022. [CrossRef]
38. Tumor, I.Y.; Thompson, D.C.; Wood, K.L.; Crawford, R.H. Characterization of surface fault patterns with application to a layered manufacturing process. *J. Manuf. Syst.* **1998**, *17*, 23–36. [CrossRef]
39. Greiner, S.; Lanzl, L.; Zhao, M.; Wudy, K.; Drummer, D. Influence of powder bed surface on part properties produced by selective laser beam melting of polymers. In Proceedings of the 7th International Congress on Architectural Technology (ICAT 2018), Maribor, Slovenia, 14–17 June 2018; pp. 153–161.
40. Wudy, K. *Alterungsverhalten von Polyamid12 Beim Selektiven Lasersintern*; Lehrstuhl für Kunststofftechnik: Erlangen, Germany, 2017.